Measurement of ψ(2S) nuclear modification at backward and forward rapidity in p+p, p+Al, and p+Au collisions at √sNN=200 GeV

(PHENIX Collaboration) Acharya, U. A.; Aidala, C.; Akiba, Y.; Alfred, M.; Andrieux, V.; Apadula, N.; Asano, H.; Azmoun, B.; Babintsev, V.; Bandara, N. S.; ...

Measurement of $\psi(2S)$ nuclear modification at backward and forward rapidity in $p + p$, $p+$Al, and $p+$Au collisions at $\sqrt{s_{NN}} = 200$ GeV

U. A. Acharya,[20] C. Aidala,[40] Y. Akiba,[53,54,*] M. Alfred,[22] V. Andrieux,[40] N. Apadula,[27] H. Asano,[33,53] B. Azmoun,[7]
V. Babintsev,[23] N. S. Bandara,[39] K. N. Barish,[8] S. Bathe,[5,54] A. Bazilevsky,[7] M. Beaumier,[8] R. Belmont,[11,46] A. Berdnikov,[56]
Y. Berdnikov,[56] L. Bichon,[64] B. Blankenship,[64] D. S. Blau,[32,43] J. S. Bok,[45] V. Borisov,[56] M. L. Brooks,[35] J. Bryslawskyj,[5,8]
V. Bumazhnov,[23] S. Campbell,[12] V. Canoa Roman,[59] R. Cervantes,[59] M. Chiu,[7] C. Y. Chi,[12] I. J. Choi,[24] J. B. Choi,[29,†]
Z. Citron,[65] M. Connors,[20,54] R. Corliss,[59] Y. Corrales Morales,[35] N. Cronin,[59] T. Csörgő,[16,66] M. Csanád,[15] T. W. Danley,[47]
M. S. Daugherity,[1] G. David,[7,59] C. T. Dean,[35] K. DeBlasio,[44] K. Dehmelt,[59] A. Denisov,[23] A. Deshpande,[54,59] E. J. Desmond,[7]
A. Dion,[59] D. Dixit,[59] J. H. Do,[67] V. Doomra,[59] A. Drees,[59] K. A. Drees,[6] J. M. Durham,[35] A. Durum,[23] H. En'yo,[53]
A. Enokizono,[53,55] R. Esha,[59] S. Esumi,[63] B. Fadem,[41] W. Fan,[59] N. Feege,[59] D. E. Fields,[44] M. Finger, Jr.,[9] M. Finger,[9]
D. Fitzgerald,[40] S. L. Fokin,[32] J. E. Frantz,[47] A. Franz,[7] A. D. Frawley,[19] Y. Fukuda,[63] P. Gallus,[13] C. Gal,[59] P. Garg,[3,59]
H. Ge,[59] M. Giles,[59] F. Giordano,[24] Y. Goto,[53,54] N. Grau,[2] S. V. Greene,[64] M. Grosse Perdekamp,[24] T. Gunji,[10] H. Guragain,[20]
T. Hachiya,[42,53,54] J. S. Haggerty,[7] K. I. Hahn,[17] H. Hamagaki,[10] H. F. Hamilton,[1] J. Hanks,[59] S. Y. Han,[17,31] M. Harvey,[61]
S. Hasegawa,[28] T. O. S. Haseler,[20] T. K. Hemmick,[59] X. He,[20] J. C. Hill,[27] K. Hill,[11] A. Hodges,[20] R. S. Hollis,[8] K. Homma,[21]
B. Hong,[31] T. Hoshino,[21] N. Hotvedt,[27] J. Huang,[7] K. Imai,[28] M. Inaba,[63] A. Iordanova,[8] D. Isenhower,[1] D. Ivanishchev,[51]
B. V. Jacak,[59] M. Jezghani,[20] X. Jiang,[35] Z. Ji,[59] B. M. Johnson ⓘ,[7,20] D. Jouan,[49] D. S. Jumper,[24] J. H. Kang,[67]
D. Kapukchyan,[8] S. Karthas,[59] D. Kawall,[39] A. V. Kazantsev,[32] V. Khachatryan,[59] A. Khanzadeev,[51] A. Khatiwada,[35]
C. Kim,[8,31] E.-J. Kim,[29] M. Kim,[57] T. Kim,[17] D. Kincses,[15] A. Kingan,[59] E. Kistenev,[7] J. Klatsky,[19] P. Kline,[59] T. Koblesky,[11]
D. Kotov,[51,56] L. Kovacs,[15] S. Kudo,[63] K. Kurita,[55] Y. Kwon,[67] J. G. Lajoie,[27] D. Larionova,[56] A. Lebedev,[27] S. Lee,[67]
S. H. Lee,[27,40,59] M. J. Leitch,[35] Y. H. Leung,[59] N. A. Lewis,[40] S. H. Lim,[35,52,67] M. X. Liu,[35] X. Li,[35] V.-R. Loggins,[24]
D. A. Loomis,[40] K. Lovasz,[14] D. Lynch,[7] S. Lökös,[15] T. Majoros,[14] Y. I. Makdisi,[6] M. Makek,[68] V. I. Manko,[32] E. Mannel,[7]
M. McCumber,[35] P. L. McGaughey,[35] D. McGlinchey,[11,35] C. McKinney,[24] C. Mendoza,[8] A. C. Mignerey,[38] A. Milov,[65]
D. K. Mishra,[4] J. T. Mitchell,[7] M. Mitrankova,[56] Iu. Mitrankov,[56] G. Mitsuka,[30,54] S. Miyasaka,[53,62] S. Mizuno,[53,63]
M. M. Mondal,[59] P. Montuenga,[24] T. Moon,[31,67] D. P. Morrison,[7] B. Mulilo,[31,53,69] T. Murakami,[33,53] J. Murata,[53,55] K. Nagai,[62]
K. Nagashima,[21] T. Nagashima,[55] J. L. Nagle,[11] M. I. Nagy,[15] I. Nakagawa,[53,54] K. Nakano,[53,62] C. Nattrass,[60] S. Nelson,[18]
T. Niida,[63] R. Nouicer,[7,54] T. Novák,[16,66] N. Novitzky,[59,63] G. Nukazuka,[53,54] A. S. Nyanin,[32] E. O'Brien,[7] C. A. Ogilvie,[27]
J. D. Orjuela Koop,[11] J. D. Osborn,[40,48] A. Oskarsson,[36] G. J. Ottino,[44] K. Ozawa,[30,63] V. Pantuev,[25] V. Papavassiliou,[45]
J. S. Park,[57] S. Park,[53,57,59] M. Patel,[27] S. F. Pate,[45] W. Peng,[64] D. V. Perepelitsa,[7,11] G. D. N. Perera,[45] D. Yu. Peressounko,[32]
C. E. PerezLara,[59] J. Perry,[27] R. Petti,[7] M. Phipps,[7,24] C. Pinkenburg,[7] R. P. Pisani,[7] M. Potekhin,[7] A. Pun,[47] M. L. Purschke,[7]
P. V. Radzevich,[56] N. Ramasubramanian,[59] K. F. Read,[48,60] D. Reynolds,[58] V. Riabov,[43,51] Y. Riabov,[51,56] D. Richford,[5]
T. Rinn,[24,27] S. D. Rolnick,[8] M. Rosati,[27] Z. Rowan,[5] J. Runchey,[27] A. S. Safonov,[56] T. Sakaguchi,[7] H. Sako,[28]
V. Samsonov,[43,51] M. Sarsour,[20] S. Sato,[28] B. Schaefer,[64] B. K. Schmoll,[60] K. Sedgwick,[8] R. Seidl,[53,54] A. Sen,[27,60] R. Seto,[8]
A. Sexton,[38] D. Sharma,[59] I. Shein,[23] M. Shibata,[42] T.-A. Shibata,[53,62] K. Shigaki,[21] M. Shimomura,[27,42] T. Shioya,[63]
P. Shukla,[4] A. Sickles,[24] C. L. Silva,[35] D. Silvermyr,[36] B. K. Singh,[3] C. P. Singh,[3] V. Singh,[3] M. Slunečka,[9] K. L. Smith,[19]
M. Snowball,[35] R. A. Soltz,[34] W. E. Sondheim,[35] S. P. Sorensen,[60] I. V. Sourikova,[7] P. W. Stankus,[48] S. P. Stoll,[7] T. Sugitate,[21]
A. Sukhanov,[7] T. Sumita,[53] J. Sun,[59] Z. Sun,[14] J. Sziklai,[66] R. Takahama,[42] K. Tanida,[28,54,57] M. J. Tannenbaum,[7]
S. Tarafdar,[64,65] A. Taranenko,[43] G. Tarnai,[14] R. Tieulent,[20,37] A. Timilsina,[27] T. Todoroki,[53,54,63] M. Tomášek,[13] C. L. Towell,[1]
R. S. Towell,[1] I. Tserruya,[65] Y. Ueda,[21] B. Ujvari,[14] H. W. van Hecke,[35] J. Velkovska,[64] M. Virius,[13] V. Vrba,[13,26] N. Vukman,[68]
X. R. Wang,[45,54] Y. S. Watanabe,[10] C. P. Wong,[20,35] C. L. Woody,[7] L. Xue,[20] C. Xu,[45] Q. Xu,[64] S. Yalcin,[59] Y. L. Yamaguchi,[59]
H. Yamamoto,[63] A. Yanovich,[23] I. Yoon,[57] J. H. Yoo,[31] I. E. Yushmanov,[32] H. Yu,[45,50] W. A. Zajc,[12] A. Zelenski,[6] and L. Zou[8]

(PHENIX Collaboration)

[1]*Abilene Christian University, Abilene, Texas 79699, USA*
[2]*Department of Physics, Augustana University, Sioux Falls, South Dakota 57197, USA*
[3]*Department of Physics, Banaras Hindu University, Varanasi 221005, India*
[4]*Bhabha Atomic Research Centre, Bombay 400 085, India*
[5]*Baruch College, City University of New York, New York, New York, 10010 USA*
[6]*Collider-Accelerator Department, Brookhaven National Laboratory, Upton, New York 11973-5000, USA*
[7]*Physics Department, Brookhaven National Laboratory, Upton, New York 11973-5000, USA*
[8]*University of California-Riverside, Riverside, California 92521, USA*
[9]*Charles University, Ovocný trh 5, Praha 1, 116 36, Prague, Czech Republic*

---

*akiba@rcf.rhic.bnl.gov
†Deceased.

[10]*Center for Nuclear Study, Graduate School of Science, University of Tokyo, 7-3-1 Hongo, Bunkyo, Tokyo 113-0033, Japan*

[11]*University of Colorado, Boulder, Colorado 80309, USA*

[12]*Columbia University, New York, New York 10027 and Nevis Laboratories, Irvington, New York 10533, USA*

[13]*Czech Technical University, Zikova 4, 166 36 Prague 6, Czech Republic*

[14]*Debrecen University, H-4010 Debrecen, Egyetem tér 1, Hungary*

[15]*ELTE, Eötvös Loránd University, H-1117 Budapest, Pázmány P. s. 1/A, Hungary*

[16]*Eszterházy Károly University, Károly Róbert Campus, H-3200 Gyöngyös, Mátrai út 36, Hungary*

[17]*Ewha Womans University, Seoul 120-750, Korea*

[18]*Florida A&M University, Tallahassee, Florida 32307, USA*

[19]*Florida State University, Tallahassee, Florida 32306, USA*

[20]*Georgia State University, Atlanta, Georgia 30303, USA*

[21]*Hiroshima University, Kagamiyama, Higashi-Hiroshima 739-8526, Japan*

[22]*Department of Physics and Astronomy, Howard University, Washington, DC 20059, USA*

[23]*IHEP Protvino, State Research Center of Russian Federation, Institute for High Energy Physics, Protvino, 142281, Russia*

[24]*University of Illinois at Urbana-Champaign, Urbana, Illinois 61801, USA*

[25]*Institute for Nuclear Research of the Russian Academy of Sciences, prospekt 60-letiya Oktyabrya 7a, Moscow 117312, Russia*

[26]*Institute of Physics, Academy of Sciences of the Czech Republic, Na Slovance 2, 182 21 Prague 8, Czech Republic*

[27]*Iowa State University, Ames, Iowa 50011, USA*

[28]*Advanced Science Research Center, Japan Atomic Energy Agency, 2-4 Shirakata Shirane, Tokai-mura, Naka-gun, Ibaraki-ken 319-1195, Japan*

[29]*Jeonbuk National University, Jeonju, 54896, Korea*

[30]*KEK, High Energy Accelerator Research Organization, Tsukuba, Ibaraki 305-0801, Japan*

[31]*Korea University, Seoul 02841, Korea*

[32]*National Research Center "Kurchatov Institute," Moscow, 123098 Russia*

[33]*Kyoto University, Kyoto 606-8502, Japan*

[34]*Lawrence Livermore National Laboratory, Livermore, California 94550, USA*

[35]*Los Alamos National Laboratory, Los Alamos, New Mexico 87545, USA*

[36]*Department of Physics, Lund University, Box 118, SE-221 00 Lund, Sweden*

[37]*IPNL, CNRS/IN2P3, Univ Lyon, Université Lyon 1, F-69622, Villeurbanne, France*

[38]*University of Maryland, College Park, Maryland 20742, USA*

[39]*Department of Physics, University of Massachusetts, Amherst, Massachusetts 01003-9337, USA*

[40]*Department of Physics, University of Michigan, Ann Arbor, Michigan 48109-1040, USA*

[41]*Muhlenberg College, Allentown, Pennsylvania 18104-5586, USA*

[42]*Nara Women's University, Kita-uoya Nishi-machi Nara 630-8506, Japan*

[43]*National Research Nuclear University, MEPhI, Moscow Engineering Physics Institute, Moscow, 115409, Russia*

[44]*University of New Mexico, Albuquerque, New Mexico 87131, USA*

[45]*New Mexico State University, Las Cruces, New Mexico 88003, USA*

[46]*Physics and Astronomy Department, University of North Carolina at Greensboro, Greensboro, North Carolina 27412, USA*

[47]*Department of Physics and Astronomy, Ohio University, Athens, Ohio 45701, USA*

[48]*Oak Ridge National Laboratory, Oak Ridge, Tennessee 37831, USA*

[49]*IPN-Orsay, Univ. Paris-Sud, CNRS/IN2P3, Université Paris-Saclay, BP1, F-91406, Orsay, France*

[50]*Peking University, Beijing 100871, People's Republic of China*

[51]*PNPI, Petersburg Nuclear Physics Institute, Gatchina, Leningrad region, 188300, Russia*

[52]*Pusan National University, Pusan 46241, Korea*

[53]*RIKEN Nishina Center for Accelerator-Based Science, Wako, Saitama 351-0198, Japan*

[54]*RIKEN BNL Research Center, Brookhaven National Laboratory, Upton, New York 11973-5000, USA*

[55]*Physics Department, Rikkyo University, 3-34-1 Nishi-Ikebukuro, Toshima, Tokyo 171-8501, Japan*

[56]*Saint Petersburg State Polytechnic University, St. Petersburg, 195251 Russia*

[57]*Department of Physics and Astronomy, Seoul National University, Seoul 151-742, Korea*

[58]*Chemistry Department, Stony Brook University, SUNY, Stony Brook, New York 11794-3400, USA*

[59]*Department of Physics and Astronomy, Stony Brook University, SUNY, Stony Brook, New York 11794-3800, USA*

[60]*University of Tennessee, Knoxville, Tennessee 37996, USA*

[61]*Texas Southern University, Houston, Texas 77004, USA*

[62]*Department of Physics, Tokyo Institute of Technology, Oh-okayama, Meguro, Tokyo 152-8551, Japan*

[63]*Tomonaga Center for the History of the Universe, University of Tsukuba, Tsukuba, Ibaraki 305, Japan*

[64]*Vanderbilt University, Nashville, Tennessee 37235, USA*

[65]*Weizmann Institute, Rehovot 76100, Israel*

[66]*Institute for Particle and Nuclear Physics, Wigner Research Centre for Physics, Hungarian Academy of Sciences (Wigner RCP, RMKI) H-1525 Budapest 114, POBox 49, Budapest, Hungary*

[67]*Yonsei University, IPAP, Seoul 120-749, Korea*

[68]*Department of Physics, Faculty of Science, University of Zagreb, Bijenička c. 32 HR-10002 Zagreb, Croatia*

[69]*Department of Physics, School of Natural Sciences, University of Zambia, Great East Road Campus,*
Box 32379, Lusaka, Zambia

Suppression of the J/ψ nuclear-modification factor has been seen as a trademark signature of final-state effects in large collision systems for decades. In small systems, the nuclear modification was attributed to cold-nuclear-matter effects until the observation of strong differential suppression of the $\psi(2S)$ state in $p + A$ and $d + A$ collisions suggested the presence of final-state effects. Results of J/ψ and $\psi(2S)$ measurements in the dimuon decay channel are presented here for $p + p$, $p + \mathrm{Al}$, and $p + \mathrm{Au}$ collision systems at $\sqrt{s_{NN}} = 200$ GeV. The results are predominantly shown in the form of the nuclear-modification factor, R_{pA}, the ratio of the $\psi(2S)$ invariant yield per nucleon-nucleon collision in collisions of proton on target nucleus to that in $p + p$ collisions. Measurements of the J/ψ and $\psi(2S)$ nuclear-modification factor are compared with shadowing and transport-model predictions, as well as to complementary measurements at Large Hadron Collider energies.

I. INTRODUCTION

Over the last decade, hydrodynamic calculations developed for $A + A$ collisions have been extended to small collision systems. Recently, interest in small systems has surged with experimental data consistent with flow-like behavior [1–5], suggesting the possibility of hot-nuclear-matter effects in systems that were not previously believed to meet the threshold energy density for quark-gluon plasma formation (≈ 1 GeV/fm^3). In 2018, a PHENIX publication determined that elliptic and triangular-flow measurements in $p + \mathrm{Au}$, $d + \mathrm{Au}$, and $^3\mathrm{He} + \mathrm{Au}$ collisions of high event multiplicity were all consistent with hydrodynamic flow [6]. A more recent study performed using new analysis techniques has confirmed these results [7].

In $d + \mathrm{Au}$ collisions at the Relativistic Heavy Ion Collider (RHIC), preferential suppression of the quarkonia $\psi(2S)$ state was observed, which is a possible signature of final-state effects [8]. Suppression of the $\psi(2S)$ nuclear modification factor was later observed at the Large Hadron Collider (LHC) by the ALICE and LHCb collaborations in $p + \mathrm{Pb}$ collisions [9,10]. The PHENIX $\psi(2S)$ results were published following an analysis of J/ψ nuclear modification in $d + \mathrm{Au}$ collisions, which indicated cold-nuclear-matter (CNM) effects were responsible for the modification of J/ψ production [11]. CNM effects are collectively known as any modification to charmonium production not caused by a hot and dense medium produced in the collision [12]. Modifications to the gluon-nuclear-parton distribution functions (nPDFs) in the nucleus [13,14], nuclear absorption (nuclear break up) [15,16], parton energy loss [17], and the Cronin effect [18] are examples of CNM effects. At LHC energies, similar J/ψ modification results were published in $p + \mathrm{Pb}$ collisions [19,20] and were also primarily consistent with CNM effects.

There is still an open debate within the community about the exact definition of initial- and final-state effects. In particular, there is some ambiguity about whether nuclear absorption should be defined as an initial- or final-state effect.

Throughout this paper, "initial-state effects" are CNM effects, including nuclear absorption, and "final-state effects" are due to the energy produced during the collision.

The initial- and final-state effects are expected to be different at RHIC and LHC energies, so the comparison of PHENIX with LHC measurements is particularly valuable. In general, J/ψ nuclear modification across the different experiments appears consistent with CNM effects, while the suppression observed in $\psi(2S)$ nuclear modification is stronger with respect to the J/ψ nuclear modification than predicted by CNM effects.

Charmonium results have been published at LHC energies by the ATLAS, ALICE, LHCb, and CMS experiments in $p + \mathrm{Pb}$ collisions at $\sqrt{s_{NN}} = 5.02$ TeV. The ATLAS collaboration has reported J/ψ [21] and charmonium [22] measurements. The J/ψ [19,20] and $\psi(2S)$ [9,23] nuclear modification has been published by the ALICE collaboration, and more recently [24] at $\sqrt{s_{NN}} = 8.16$ TeV. The LHCb collaboration has measured J/ψ [25] and $\psi(2S)$ [10]. Lastly, J/ψ [26] and $\psi(2S)$ [27] measurements were published by the CMS collaboration.

At RHIC energies, J/ψ and $\psi(2S)$ production was studied in $p + p$, $p + \mathrm{Al}$, $p + \mathrm{Au}$, $d + \mathrm{Au}$, and $^3\mathrm{He} + \mathrm{Au}$ collisions at $\sqrt{s_{NN}} = 200$ GeV. PHENIX has published J/ψ measurements at $|y| < 0.35$ and $1.2 < |y| < 2.2$ in $p + p$ collisions [28] and $d + \mathrm{Au}$ collisions [11,29]. At backward and forward rapidity $1.2 < |y| < 2.2$, PHENIX has published J/ψ nuclear modification in $p + \mathrm{Al}$, $p + \mathrm{Au}$, and $^3\mathrm{He} + \mathrm{Au}$ collisions [30]. The J/ψ nuclear modification in $d + \mathrm{Au}$ collisions was measured by the STAR collaboration at rapidity $|y| < 1$ [31]. The $\psi(2S)$ nuclear-modification factor was also measured by PHENIX in $d + \mathrm{Au}$ collisions at rapidity $|y| < 0.35$ [8], and the $\psi(2S)$ to J/ψ ratio for the centrality-integrated case was measured in $p + p$, $p + \mathrm{Al}$, $p + \mathrm{Au}$, and $^3\mathrm{He} + \mathrm{Au}$ collisions at rapidity $1.2 < |y| < 2.2$ [32]. The results presented in this paper provide the first measurements at RHIC of the $\psi(2S)$ nuclear-modification factor and its centrality dependence at backward and forward rapidity.
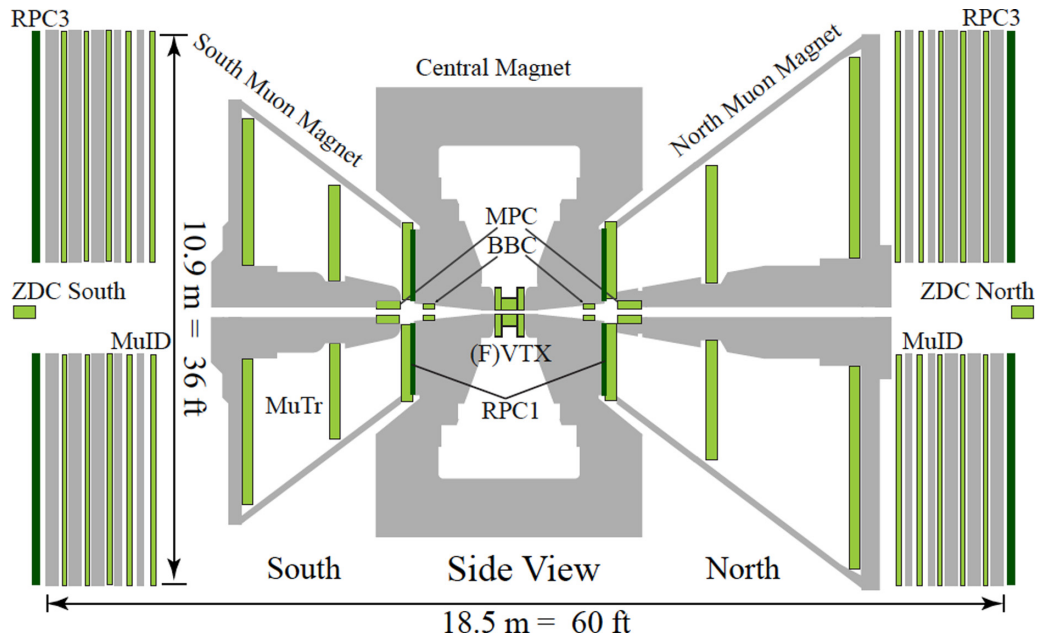
FIG. 1. Side view of the PHENIX detector as configured for recording of data in 2015.

II. EXPERIMENTAL SETUP

A. The muon arms

The PHENIX muon arms measure muons and unidentified-charged hadrons at backward and forward rapidity. Covering the full azimuthal angle, the muon arms comprise four main components: The forward silicon vertex (FVTX), the muon tracker (MuTr), the muon identifier (MuID), and hadron absorbers [33–36].

Installed in 2012, the FVTX detector is a precision silicon detector comprising two identical endcaps containing four layers of active silicon sensors surrounding a barrel silicon vertex (VTX) detector. As shown in Fig. 1, the FVTX is situated between the first hadron absorber and the collision region and provides an additional space point for muon-arms track reconstruction. The location of the FTVX detector is critical, as particles traveling through the hadron absorbers experience multiple scattering, which impacts the mass resolution of dimuon pairs due to a less precise pair opening angle measurement. The FVTX detector used in the analysis is essential for extracting the $\psi(2S)$ signal.

The PHENIX MuTr covers a pseudorapidity range of $-2.2 < \eta < -1.2$ at backward rapidity and $1.2 < \eta < 2.4$ at forward rapidity. The MuTr comprises three individual cathode strip chambers called stations that face perpendicular to the direction of the beam. Particles bend in the azimuthal direction under the $\oint \mathbf{B} \cdot d\mathbf{l} = 0.72$ T m magnetic field as they leave the interaction point. Signals induced on the cathode strips are used to reconstruct the trajectory of each particle.

The MuID is located outside the muon-arms magnetic field and directly behind the MuTr with respect to the collision vertex. Particles travel in straight trajectories through five alternating layers of multiwire chambers and hadronic absorbers called *gaps*, where gap 0 is closest to the interac-

tion point. The total hadronic absorber thickness along the beamline is 90 cm (80 cm) in the MuID north (south) arms. A MuID absorber thickness of 90 cm corresponds to a 3% probability for punch-through hadrons with maximum momenta of 4 GeV/c.

The hadron absorbers closest to the collision region are the 60-cm-thick central magnet and 20-cm-thick copper nose cones. Two additional 35-cm-thick stainless-steel absorbers run along the surface of the magnet at backward and forward rapidity. The MuID and the MuTr are divided by the muon-magnet yoke, which serves as a steel absorber 30 cm (20 cm) thick at forward (backward) rapidity. The MuID includes an additional 80 cm of steel absorbers. The total thickness of hadron-absorber material is 225 cm (215 cm) in the north (south) muon arms.

Two beam-beam counters (BBCs) are positioned inside an ≈ 0.3 T magnetic-field region on both sides of the interaction point along the beamline. A Čerenkov array detector, the BBC detectors comprise 128 identical quartz photomultiplier tubes. The acceptance for the BBC is full azimuthal angle and $3.1 < |\eta| < 3.9$ in pseudorapidity. The BBC is used to determine the vertex position along the direction of the beam, and PHENIX also classifies the event centrality using the total charge recorded in the BBC. In small systems, the centrality is determined using only the backward rapidity BBC charge. The BBC was also used to measure the beam luminosity and form a minimum bias (MB) trigger. Also shown in Fig. 1 are the resistive-plate chambers (RPCs) and the muon-piston calorimeter (MPC), used in geometry-related PHENIX measurements, which were not used in this analysis.

A Monte Carlo Glauber model calculation is used to determine the centrality categorization. Values such as the inelastic nucleon-nucleon cross section and the nuclear charge density are input into the Glauber model, which simulates the probability of collision between nuclei based on the

TABLE I. The mean number of binary-binary collisions ($\langle N_{\mathrm{coll}} \rangle$) and bias correction factors (c_{BBC}) determined from Glauber model calculations [37] for the different $p + \mathrm{Al}$ and $p + \mathrm{Au}$ collision-centrality classes.

Collision system	Centrality	$\langle N_{\mathrm{coll}} \rangle$	c_{BBC}
$p + \mathrm{Al}$	0%–100%	2.1 ± 0.1	0.80 ± 0.02
$p + \mathrm{Au}$	0%–20%	8.2 ± 0.5	0.90 ± 0.01
	20%–40%	6.1 ± 0.4	0.98 ± 0.01
	20%–84%	4.3 ± 0.3	1.00 ± 0.03
	40%–84%	3.4 ± 0.2	1.01 ± 0.04
	0%–100%	4.7 ± 0.3	0.86 ± 0.01

nucleon-nucleon inelastic cross section. The total amount of charge in the BBC detector in the A-going direction ($-3.9 < \eta < -3.1$) is used to define the centrality classes in small collision systems. $\langle N_{\mathrm{coll}} \rangle$, the mean number of binary (or nucleon-nucleon) collisions, for each centrality range are extracted from the Glauber model [37]. The bias in the centrality measurement due to the presence of a hard process in the collision is accounted for by applying the c_{BBC} correction. Table I lists the centrality classes and the $\langle N_{\mathrm{coll}} \rangle$ and bias correction factors c_{BBC} for the $p + \mathrm{Al}$ and $p + \mathrm{Au}$ data sets.

III. DATA ANALYSIS

A. Data set

Three different small system data sets were analyzed for the $\psi(2S)$ measurements: $p + p$, $p + \mathrm{Al}$, and $p + \mathrm{Au}$ collisions recorded during the 2015 run year, all at a center-of-mass energy of $\sqrt{s_{NN}} = 200$ GeV. The corresponding integrated luminosities are 23 pb^{-1}, 260 nb^{-1}, and 138 nb^{-1} for the $p + p$, $p + \mathrm{Al}$, and $p + \mathrm{Au}$ data sets, respectively. Forward rapidity results ($1.2 < y < 2.2$) correspond to the p-going direction, while backward rapidity results ($-2.2 < y < -1.2$) correspond to the Al- and Au-going direction. Analyzed J/ψ and $\psi(2S)$ events were selected with a dimuon trigger that fires when two particles penetrate gap 3 in the MuID.

B. Dimuon track selection

The FVTX detector and the MuTr are both used for dimuon analysis in the PHENIX muon arms. The $J/\psi \rightarrow \mu^+ \mu^-$ decay channel has a large signal-to-background ratio, and the MuTr momentum resolution is sufficient for J/ψ analysis. However, the MuTr momentum resolution is insufficient to extract the $\psi(2S)$ yields, which are approximately 3% of the J/ψ signal. The FVTX detector provides additional space points near the collision vertex before the particle begins its trajectory through the muon-arm absorbers, enhancing the mass resolution.

A dimuon pair is composed of single muons (Muon1 and Muon2) identified by the MuTr and FVTX detectors. Four cases are listed below:

(1) MuTr + MuTr (no FVTX-match requirement);
(2) FVTX + MuTr (single FVTX-matched pair required);

(3) FVTX + FVTX (double FVTX-matched pair required);
(4) the sum of cases 2 + 3.

Case 1 was used in the recent J/ψ analysis with the same data sets for better statistics [30]. Case 2, the single FVTX-matched pair, comprises a dimuon pair formed from one MuTr only track and one FVTX associated track. Case 3, the double FVTX-matched pair, comprises a dimuon pair formed from two FVTX associated tracks. The $\psi(2S)$ results presented in this paper have used Case 4, which is the sum of single + double FVTX-matched pairs.

C. $\psi(2S)$ signal extraction

The crystal-ball (CB) function [38] and the modified-Hagedorn function [39,40] were used to fit dimuon invariant-mass distributions. The CB function combines a power-law function with a Gaussian function [38]. The momentum resolution of the detector dominates the width of the J/ψ and $\psi(2S)$ peaks, and the energy loss due to multiple scattering is modeled by the power-law tail. The CB function along with the expanded parameters A and B for the power-law tail is shown in Eq. (1):

$$
\begin{aligned}
f(m) &= N \exp\left(-\frac{(m - \bar{m})^2}{2\sigma^2} \right) \quad \text{for } \frac{m - \bar{m}}{\sigma} > \alpha, \\
f(m) &= NA\left(B - \frac{(m - \bar{m})^2}{2\sigma^2} \right) \quad \text{for } \frac{m - \bar{m}}{\sigma} \leqslant \alpha, \\
A &= \left(\frac{n}{|\alpha|} \right)^n \exp\left(-\frac{|\alpha|^2}{2} \right), \\
B &= \frac{n}{|\alpha|} - |\alpha|,
\end{aligned}
\tag{1}
$$

The mass centroid and width of the J/ψ peak allowed us to vary in the centrality-integrated measurements. To ensure fit stability in the finer centrality bins, the centroid and width were fixed to the centrality-integrated results for measurements as a function of $\langle N_{\mathrm{coll}} \rangle$, and the CB parameters α and n were fixed to values determined from simulation (see Sec. III G 1).

Both the mass centroid and width of the $\psi(2S)$ signal were fixed in all measurements. The value of the $\psi(2S)$ width was fixed to a result previously determined by simulation and based on the muon-arms mass resolution, where the ratio of the $\psi(2S)$ to J/ψ width is expected to be 1.15 [41]. The $\psi(2S)$ mass was fixed to the J/ψ mass plus a constant value Δm, as was done in a previous PHENIX analysis [32]. The value Δm is the mass difference between the $\psi(2S)$ and J/ψ states, as reported by the Particle Data Group [42]. See Sec. III G for a discussion of the systematic uncertainty associated with fixing the $\psi(2S)$ lineshape.

In addition to the CB, a second Gaussian curve was used in the total fit function to reproduce the high-mass tail seen in Fig. 2. Misassociated tracks between the MuTr and the FVTX detectors can create this effect which is not observed in dimuon analyses, where only MuTr information is used. The parameters for the second Gaussian were determined in
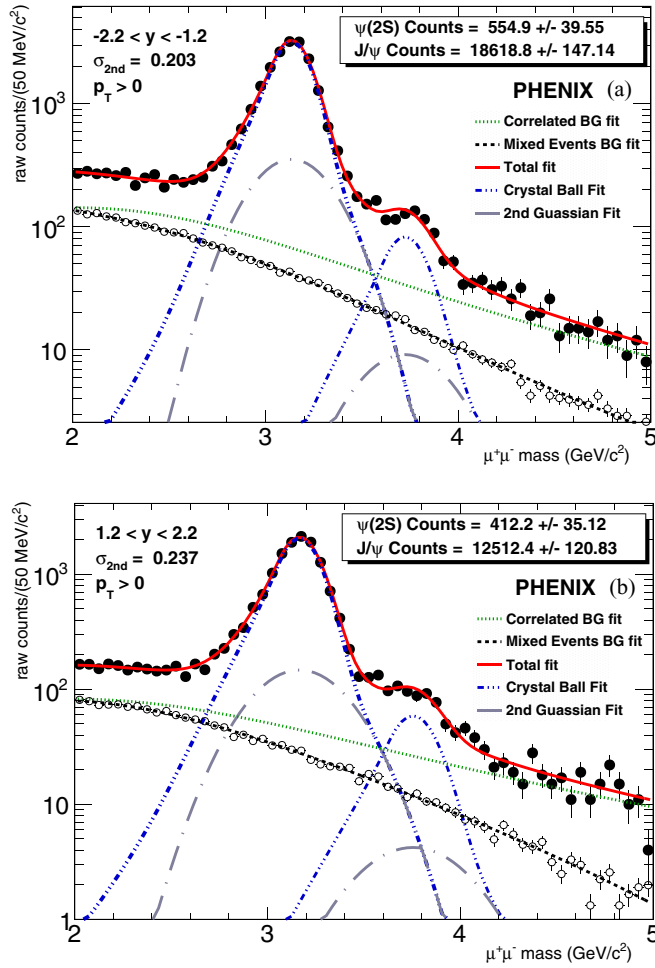
FIG. 2. The p_T-integrated dimuon invariant-mass spectrum in $p + p$ collisions at (a) backward and (b) forward rapidity. A CB function with a second Gaussian was used to extract the signals, and a modified-Hagedorn function was used to estimate the background contribution.

simulation and verified using a toy-model study that is discussed in more detail below.

The second Gaussian function contains three parameters: $\bar{m}_{2nd}$, σ_{2nd}, and N_{2nd}, which correspond to the mass centroid, width, and normalization of the curve. Based on the previous PHENIX muon-arms analysis [32], the following second Gaussian parameter constraints are assumed:

$$f = f', \quad r = r', \quad \bar{m} = \bar{m}_{2nd}, \quad \bar{m}' = \bar{m}'_{2nd}, \qquad (2)$$

where $f = \frac{N_{2nd}}{N}$ is the ratio of the J/ψ second Gaussian normalization to the CB normalization, $f' = \frac{N'_{2nd}}{N'}$ is the ratio of the $\psi(2S)$ second Gaussian normalization to the CB normalization, $r = \frac{\sigma_{2nd}}{\sigma}$ is the ratio of the J/ψ second Gaussian width to the CB width, $r' = \frac{\sigma'_{2nd}}{\sigma'}$ is the ratio of the $\psi(2S)$ second Gaussian width to the CB width, $\bar{m}_{2nd}$ is the J/ψ second Gaussian mass centroid, $\bar{m}'_{2nd}$ is the $\psi(2S)$ second Gaussian mass centroid, $\bar{m}$ is the J/ψ CB mass centroid, and $\bar{m}'$ is the $\psi(2S)$ CB mass centroid. The ratios f and r were determined from fits to the simulated J/ψ mass distribution

using embedded simulations with high statistics. The ratios f and r were then used in real data analysis by multiplying them with the corresponding free parameter in the total fit function following the constraints given in Eq. (2).

To summarize the total fit function, there are fixed parameters included to stabilize the fit: three parameters in the correlated background; two parameters (mean and sigma) in the $\psi(2S)$ CB function; the ratio of mean and sigma between the CB function and the second Gaussian function; α and n in the CB tail parameters only for centrality-dependent fits based on the parameters from the integrated-centrality fits. All fixed-parameter values are different for collision systems and rapidity ranges, except for the $\psi(2S)$ mass and width parameter values.

D. Background estimation

A mixed-events background was generated to approximate the random-combinatorial-background contribution to the dimuon-invariant mass spectrum by selecting oppositely charged single muons $\mu^+\mu^-$ from different events. An event pool of four events was used to reduce the statistical uncertainty of the mixed-events background. All generated mixed events must be within 2 cm of the z vertex and come from the same centrality class as the main event.

The correlated background comprises contributions from Drell-Yan, charm, bottom, and charged hadron dimuon pairs. The correlated-background shape is not precisely known at the muon-arm acceptance. The same approach was followed as in the recent analysis [30]. A modified-Hagedorn function was included in the total fit function to estimate the correlated-background contribution, and the shape was constrained based on detailed simulation studies of all components [39,43]. The modified Hagedorn is given as

$$\frac{d^2N}{dm_{\mu\mu}dp_T} = \frac{p_0}{\left[\exp\left(-p_1 m_{\mu\mu} - p_2 m_{\mu\mu}^2\right) + m_{\mu\mu}/p_3\right]^{p_4}}, \qquad (3)$$

where p_0 is the normalization parameter, p_4 is the high-mass tail parameter, $m_{\mu\mu}$ is the reconstructed dimuon mass, and p_1, p_2, and p_3 are fit parameters. In the fits to the real data, the parameters p_0, p_1, and p_3 were fixed to values determined by the simulation studies, while the remaining parameters p_2 and p_4 were not fixed. The systematic uncertainty associated with this approach is discussed in Sec. III G.

E. Efficiency correction

The combined acceptance and reconstruction efficiency correction is applied to the dimuon invariant yield to compensate for the geometric acceptance of the detector and the track-reconstruction efficiency. This correction was determined using simulations, where J/ψ or $\psi(2S)$ candidates were generated with PYTHIA8 [44] and thrown into the geometric acceptance region of the PHENIX muon arms. The simulated events were embedded into real physics data to account for the effects of background hits for $p + A$ collisions. A full detector simulation was performed using GEANT4 [45], and includes a dimuon trigger emulator for the trigger-efficiency determination. The acceptance and

reconstruction efficiency corrections for $\psi(2S)$ in $p + p$ collisions are $\approx 3.5\%$ and $\approx 4.5\%$ at backward and forward rapidity, respectively, for the requirement of at least one FVTX + MuTr matching. In comparison, the J/ψ acceptance and reconstruction efficiency corrections in $p + p$ collisions are $\approx 3.0\%$ and $\approx 3.5\%$ at the same rapidities. The higher acceptance and reconstruction efficiency for the $\psi(2S)$ is expected due to its larger mass. In centrality-integrated $p + Au$ collisions, the $\psi(2S)$ acceptance and reconstruction efficiency is $\approx 3.0\%$ and $\approx 4.0\%$ at backward and forward rapidities.

F. Nuclear modification factor

The dimuon invariant yield for a given rapidity, centrality, and p_T in a certain collision system is given as

$$B_{\mu\mu} \frac{d^2 Y^{\mu\mu}}{d p_T d y} = \frac{1}{2\pi p_T \Delta p_T \Delta y} \frac{\epsilon_{\mathrm{BBC}} N^{\mu\mu}}{\epsilon_{\mathrm{trig}} \epsilon_{\mathrm{Ae}} N_{\mathrm{MB}}}, \qquad (4)$$

where $N^{\mu\mu}$ is the number of raw (uncorrected) J/ψ or $\psi(2S)$ counts per bin, $B_{\mu\mu}$ is the branching ratio to dimuons, ϵ_{trig} and ϵ_{Ae} are the dimuon trigger and combined acceptance and reconstruction efficiencies, p_T is the center of the p_T bin, Δp_T is the p_T bin width, Δy is the rapidity bin width, and N_{MB} is the raw number of MB events. The BBC efficiencies for MB events and hard-scattering events are included in ϵ_{BBC}, and the list of correction factors for various centrality ranges in $p + A$ collisions is provided in Table I. For the $p + p$ data set, the BBC efficiency for MB (hard-scattering) events is 0.55 ± 0.05 (0.79 ± 0.02) [46].

The nuclear-modification factor R_{pA}, the ratio of the dimuon invariant yields in $p + A$ collisions compared with the dimuon yield in $p + p$ collisions, scaled by the average number of nucleon-nucleon collisions, is the primary observable used in the analysis:

$$R_{pA} = \frac{1}{\langle N_{\mathrm{coll}} \rangle} \frac{d^2 N^{pA}/dy dp_T}{d^2 N^{pp}/dy dp_T}, \qquad (5)$$

where $\langle N_{\mathrm{coll}} \rangle$ is the average number of nucleon-nucleon collisions per event, and $d^2 N^{pA}/dy dp_T$ and $d^2 N^{pp}/dy dp_T$ are the dimuon invariant yields in the $p + A$ and $p + p$ systems, respectively.

G. Systematic uncertainties

The systematic uncertainties are divided into three different types: Type-A, Type-B, and Type-C uncertainties. Type-A uncertainties are uncorrelated, random point-to-point uncertainties. In this paper, the Type-A uncertainties are associated with the extracted dimuon yields and are added in quadrature to statistical uncertainties. Type-B uncertainties are correlated point-to-point systematic uncertainties, and Type-C uncertainties are global uncertainties that apply uniformly to all measurements.

1. Signal extraction

After analyzing the $\psi(2S)$ invariant yield results from three different sets of analysis cuts, an outlier measurement was observed in the $p + p$ collision system. The three different sets were defined using the following criteria: Set 1 has standard

cuts for quality of track reconstruction in the MuTr, MuID, and FVTX applied, Set 2 has an additional fiducial cut applied, and Set 3 has an additional quality cut applied to the FVTX tracks. Note that Data Set 3 was used for all results presented in this paper. The outlier did not contain a probability cut, which reduces the number of misassociated tracks between the FVTX and MuTr detectors. The probability cut [47] is a FVTX track χ^2 probability (p value) quality selection cut; a probability cut of greater than 3% was applied to data Set 3. To account for the observed discrepancy in invariant yield results, the weighted averages of invariant yields from each muon arm in the three sets were compared, and the largest percent difference between them was taken as a systematic uncertainty. No outliers were observed in the comparison of the three measurements in the $p + Al$ or $p + Au$ collision systems, and no systematic uncertainty was assigned.

Aside from the probability cut, the dominant uncertainty in the $\psi(2S)$ measurements is the correlated-background uncertainty. The modified Hagedorn function shown in Eq. (3) was used to fit the estimated correlated background, as was done in a recent PHENIX analysis [30]. The shape was determined from simulation studies [39,43], and two of the five parameters in the fit function allowed us to vary. The systematic uncertainty was determined from three separate Hagedorn fits, with parameter combinations alternately fixed in each fit. Based on collision system and rapidity, variations in $\psi(2S)$ counts of 3.2%–8.4% are observed.

The modified Hagedorn function from Eq. (3) was also used to fit the mixed-events combinatorial background. An uncertainty can be introduced in the extracted yields because the mixed-events background was normalized over the same mass range used for the like-sign background. The systematic uncertainty was determined following the approach described in Ref. [32], where the mixed-events background was fit over two different mass ranges extending above and below the mass range used for the measurements. Based on collision system and rapidity, a variation in $\psi(2S)$ counts of 1.0%–3.7% are observed.

The systematic uncertainty associated with fixing the $\psi(2S)$ CB lineshape was calculated by fixing the parameter values with plus and minus twice the error in the fit results and repeating the fit. The extracted $\psi(2S)$ yields were then compared. Based on collision system and rapidity, variations in $\psi(2S)$ counts of 1.0%–1.4% are observed.

The CB tail parameters α and n were constrained to values determined by simulation. A toy-model study was used to estimate the systematic uncertainty. The mass spectra randomly generated by the toy model are based on high statistics GEANT4 simulated mass histograms as well as the relative yields of J/ψ and $\psi(2S)$ observed in real $p + p$ collision data [32]. One hundred mass distributions were produced, and the resulting yields from fitting the toy-model distributions were compared with the input J/ψ and $\psi(2S)$ counts to gauge the accuracy of the CB tail parameters. The toy model was run with α and n fixed to the initial fit result. The systematic was then determined by fixing the parameter values with plus and minus twice the error in the fit results and repeating the fits. Based on rapidity, variations in $\psi(2S)$ counts of 2.6%–3.8% are observed.

TABLE II. The $\psi(2S)$ fractional systematic uncertainties for signal extraction in $p + p$, $p + $ Al, and $p + $ Au collisions. "CB" denotes the crystal-ball fit function [38].

Source	System	Forward	Backward	Type
Prob. cut	$p + p$	9.3%	9.3%	B
Corr. bkg.	$p + p$	3.3%	3.2%	B
	$p + $ Al	7.5%	5.7%	B
	$p + $ Au	6.9%	8.4%	B
Comb. bkg.	$p + p$	<1.0%	<1.0%	B
	$p + $ Al	1.0%	1.0%	B
	$p + $ Au	1.00%	3.7%	B
Fixed CB shape	$p + p$	1.1%	1.4%	B
	$p + $ Al	1.0%	1.1%	B
	$p + $ Au	1.4%	1.4%	B
Fixed CB tail	$p + p$			B
	$p + $ Al			B
	$p + $ Au	2.6%	3.8%	B
Fit procedure	$p + p$	3.3%	3.3%	B
	$p + $ Al	2.0%	2.7%	B
	$p + $ Au	4.7%	3.3%	B

A toy model was also used to gauge the accuracy of the second Gaussian parameters f and r and the overall fit uncertainty. Fits to high statistics $\psi(2S)$ embedded simulations were used to extract the second Gaussian parameters. The toy model generates a new simulated mass distribution with each throw that was fit using the same technique as the data. Then the systematic uncertainty was calculated as the percent error between the J/ψ and $\psi(2S)$ counts input to the toy model and the averaged output of the toy model after 100 throws. Based on collision system and rapidity, variations in $\psi(2S)$ counts of 2.0%–4.7% are observed. All Type B systematic uncertainties associated with the $\psi(2S)$ and J/ψ signal extraction are summarized in Tables II and III, respectively.

2. Acceptance and efficiency correction

Both the trigger efficiency and the combined acceptance and reconstruction efficiency were determined using a full GEANT4 detector simulation. Systematic uncertainties due to

TABLE III. The 0%–100% centrality J/ψ fractional systematic uncertainties for the signal extraction in $p + p$, $p + $ Al, and $p + $ Au collisions. The J/ψ lineshapes and the CB tail parameters were not fixed for measurements in the centrality-integrated data.

Source	System	Forward	Backward	Type
Corr. bkg.	$p + p$	<1.0%	<1.0%	B
	$p + $ Al	<1.0%	<1.0%	B
	$p + $ Au	<1.0%	<1.0%	B
Comb. bkg.	$p + p$	<1.0%	<1.0%	B
	$p + $ Al	<1.0%	<1.0%	B
	$p + $ Au	<1.0%	<1.0%	B
Fit procedure	$p + p$	1.2%	1.0%	B
	$p + $ Al	1.0%	1.3%	B
	$p + $ Au	1.1%	1.4%	B

TABLE IV. The dimuon fractional systematic uncertainties in $p + p$, $p + $ Al, and $p + $ Au collisions for the combined acceptance and reconstruction efficiency correction and the trigger efficiency correction [30].

Source	System	Forward	Backward	Type
Run variation	$p + p$	4.0%	4.7%	B
	$p + $ Al	2.8%	3.3%	B
	$p + $ Au	1.6%	3.5%	B
φ matching	$p + p$	5.8%	5.0%	B
	$p + $ Al	3.6%	3.3%	B
	$p + $ Au	3.4%	4.0%	B
Initial shape	All	2.0%	2.0%	B
Trigger eff.	$p + p$	2.3%	2.6%	B
	$p + $ Al	1.0%	3.0%	B
	$p + $ Au	1.0%–4.5%	1.9%–3.5%	B

differences between data and simulation, such as the uncertainty on the MuID efficiency, were determined in a previous study [30]. The systematic uncertainties associated with the efficiency corrections are briefly summarized below.

To estimate the run-to-run variation arising from different efficiency rates, the data sets were grouped according to instantaneous beam luminosity, and the invariant yields were calculated for each group. A variation of 1.6%–4.0% was observed depending on rapidity and data set.

The φ matching systematic uncertainty due to different detector dead areas was estimated by comparing the active MuTr azimuthal angle distributions in simulation and data. A variation of 1.6%–4.7% was observed depending on rapidity and data set.

The initial-shape systematic includes the uncertainty in the simulated dimuon rapidity and p_T distributions, which are tuned to previous PHENIX measurements [11,28,29] because these distributions are not precisely known. Two sets of simulated mass distributions were compared with different assumptions of the p_T and rapidity dependence, and a systematic uncertainty of 2% is conservatively quoted for all collision systems and rapidities.

The dimuon trigger efficiency was determined from simulation using a dimuon trigger emulator. In this approach, a correction is applied to the dimuon trigger efficiency based on a comparison of the single-muon trigger efficiency obtained in simulation and real data. A variation of 1.0%–4.5% in systematic uncertainty is observed based on collision system and rapidity. All Type B systematic uncertainties associated with the dimuon acceptance and efficiency corrections are summarized in Table IV.

3. ⟨N_{coll}⟩ and beam-beam counter efficiency

The systematic uncertainty related to the mean number of nucleon-nucleon collisions, ⟨N_{coll}⟩, was determined by varying the input parameters, such as the gold nuclei Woods-Saxon parameters and the inelastic cross section of nucleon-nucleon collisions, in a Glauber-model calculation, as described in Ref. [37]. A variation of 6.1%–7.3% in systematic uncertainty is observed in $p + $ Au collisions based on centrality, as listed

in Table I. For nuclear-modification measurements as a function of $\langle N_{\text{coll}} \rangle$, the $\langle N_{\text{coll}} \rangle$ uncertainty is treated as a Type-B systematic uncertainty. The Type-C systematic uncertainty for the BBC efficiency of 10% was previously determined in $p + p$ collisions at $\sqrt{s} = 200$ GeV [48].

A previous study of multiple interactions for beam crossing in $p + p$ and $p + $Al collisions at $\sqrt{s} = 200$ GeV found approximately a 5% variation in the measured invariant yields due to the high instantaneous beam luminosity [30]. However, the acceptance and efficiency correction accounts for the instantaneous beam luminosity dependence, and a multiple interactions systematic was not quoted. The same approach is followed here.

PHENIX has recently measured the J/ψ polarization in $p + p$ collisions at midrapidity [49] and found the polarization in three different frames of reference were all consistent with zero. Additionally, LHC experiments [50–52] have found no strong evidence in favor of quarkonia polarization. Therefore, zero $\psi(2S)$ and J/ψ polarization is assumed, and a systematic uncertainty is not included for the measurements presented in this paper.

IV. RESULTS AND DISCUSSION

The $\psi(2S)$ nuclear-modification factor as a function of centrality has been compared with theoretical predictions with and without hot-nuclear-matter effects, provided by Shao *et al.* and by Du and Rapp [53]. The gluon-shadowing predictions use different parametrizations of the nPDFs, including Eskola-Paukkunen-Salgado (EPS09) [54] for the Du & Rapp predictions, and coordinated-theoretical-experimental project on QCD (nCTEQ15) [14] and Eskola-Paakkinen-Paukkunen-Salgado (EPPS16) [13] for the Shao *et al.* predictions.

Additionally, to isolate modification due to final-state effects, measuring the $\psi(2S)$ to J/ψ ratio mostly removes initial-state effects. The PHENIX $\psi(2S)$ measurements are presented alongside corresponding measurements from the ALICE and LHCb Collaborations [9,10,20,24,25].

$\psi(2S)$ results

Figure 3 shows the J/ψ and $\psi(2S)$ nuclear modification factors as a function of rapidity in $p + $Al collisions. At forward rapidity, the J/ψ and $\psi(2S)$ nuclear modification are consistent with unity, as expected based on a weaker gluon modification in the lighter aluminum target system of lower density [55]. However, at backward rapidity, suppression is seen in the $\psi(2S)$ modification with respect to the J/ψ modification. Because CNM effects are expected to be similar between the two states, nuclear absorption cannot explain the suppression at backward rapidity. The $\psi(2S)$ nuclear modification results at backward rapidity may indicate final-state effects are present in the $p + $Al system at RHIC energies; however, the sizable error bars preclude a strong conclusion. Note that a previous PHENIX publication reported a hint of collective flow in 0%–5% central $p + $Al collisions [56].

Figure 4 compares the centrality and p_T-integrated results for J/ψ and $\psi(2S)$ nuclear modification in $p + $Au collisions as a function of rapidity with both EPPS16 and

nCTEQ15 shadowing predictions provided by Shao *et al.* The J/ψ EPPS16 (nCTEQ15) predictions are also shown. These gluon-shadowing predictions by Shao *et al.* use a Bayesian-reweighting technique [57–61] for the EPPS16 and nCTEQ15 nPDFs and have a 68% confidence level. The predictions were calculated at three different factorization scales: $0.5\mu_0$, μ_0, and $2\mu_0$, where $\mu_0^2 = M^2 + p_T^2$ for the quarkonium mass (M) and transverse momentum (p_T), and the largest of the three uncertainties is quoted. Previously published PHENIX
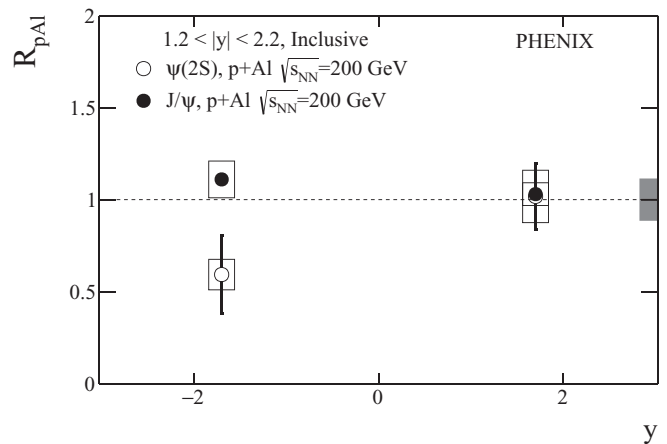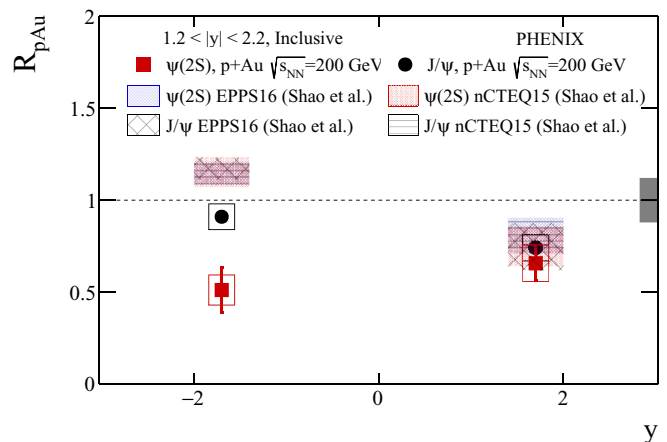

FIG. 3. The centrality and p_T-integrated $\psi(2S)$ [open circles] and J/ψ [solid circles] nuclear-modification factors as a function of rapidity in $p + $Al collisions. The error boxes (bars) represent point-to-point correlated (uncorrelated) uncertainties for each data point. The Type-C global systematic uncertainty is indicated by the shaded box on the right side of the figure and includes the BBC efficiency, $\langle N_{\text{coll}} \rangle$, and bias-correction uncertainties.

FIG. 4. The centrality and p_T-integrated $\psi(2S)$ [solid (red) squares] and J/ψ [solid (black) circles] nuclear-modification factors as a function of rapidity in $p + $Au collisions, compared with EPPS16 [13] and nCTEQ15 [14] nPDF predictions. The error boxes (bars) represent point-to-point correlated (uncorrelated) uncertainties for each data point. The Type-C global systematic uncertainty is indicated by the shaded box on the right side of the figure and includes the BBC efficiency, $\langle N_{\text{coll}} \rangle$, and bias correction uncertainties. Descriptions of the model predictions are provided in the text.
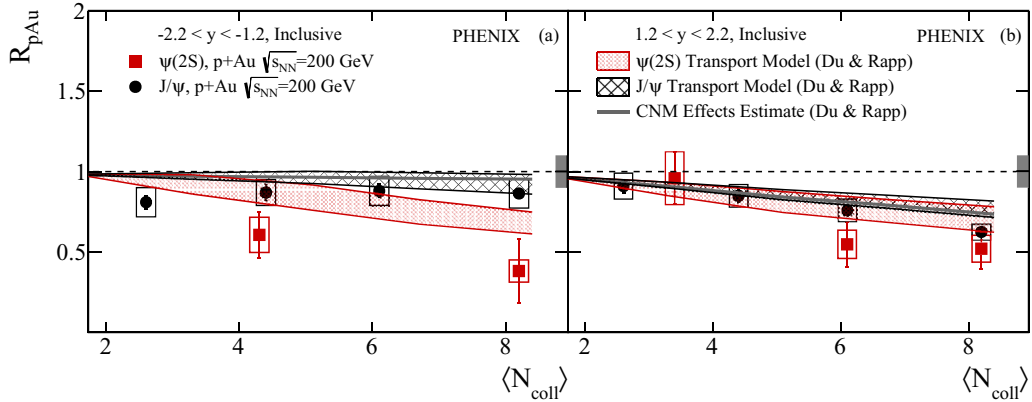
FIG. 5. The $\psi(2S)$ [solid (red) squares] and J/ψ [solid (black) circles] [24] nuclear-modification factors as a function of $\langle N_{coll} \rangle$ in $p + Au$ collisions at (a) backward and (b) forward rapidity is shown with corresponding transport-model predictions by Du and Rapp [53]. Also shown are the transport-model estimates of CNM effects, which are the same for both states. The error boxes (bars) represent point-to-point correlated (uncorrelated) uncertainties for each data point. The Type-C global systematic uncertainty is indicated by the shaded box on the right side of the figure. Descriptions of the model predictions are provided in the text.

J/ψ and $\psi(2S)$ data in $p + p$ collisions [28] were fit and used as a baseline reference. The predictions as a function of centrality used a Monte Carlo Glauber calculation [62] in addition to impact-parameter-dependent nPDF [63]. The modification at forward rapidity is well described by EPPS16 and nCTEQ15 shadowing, although the $\psi(2S)$ nuclear modification shows slightly stronger suppression than what shadowing parametrization predicts. However, at backward rapidity, both EPPS16 and nCTEQ15 nPDFs overpredict the $\psi(2S)$ nuclear-modification factor with values of 1.17 ± 0.05 and 1.19 ± 0.06, respectively, versus the measured value of 0.51 ± 0.12. Therefore, shadowing effects alone cannot describe the $\psi(2S)$ suppression observed at backward rapidity.

Figures 5 and 6 show the J/ψ [24] and $\psi(2S)$ nuclear modification measurements as a function of $\langle N_{coll} \rangle$. The nuclear modification between the two states follows a similar trend at forward rapidity, with no clear difference in suppression in the most central collisions. The $\psi(2S)$ shadowing predictions

provided by Shao *et al.* shown in Fig. 6(b) underpredict the suppression at forward rapidity. Also shown is a comparison to transport-model (TM) predictions for $\psi(2S)$ and J/ψ provided by Du and Rapp [53]. The TM was originally developed for $A + A$ collision systems [64] and has been extended to small collision systems. A nuclear-absorption estimate based on the PHENIX $d + Au$ data [8], and EPS09 shadowing effects have been included. The initial geometry of the fireball is derived from a Monte Carlo Glauber model. Gluon shadowing from the EPS09 parametrization is the dominant contribution to the TM at forward rapidity for both states. The model reproduces the relative suppression, although the degree of suppression is somewhat underpredicted. The $\psi(2S)$ TM predicts a small final-state effect, which can be seen in Fig. 5(b), where the total TM predictions and the individual contribution from CNM effects alone are shown.

A difference can be seen at backward rapidity between the J/ψ and $\psi(2S)$ nuclear modification, consistent with a
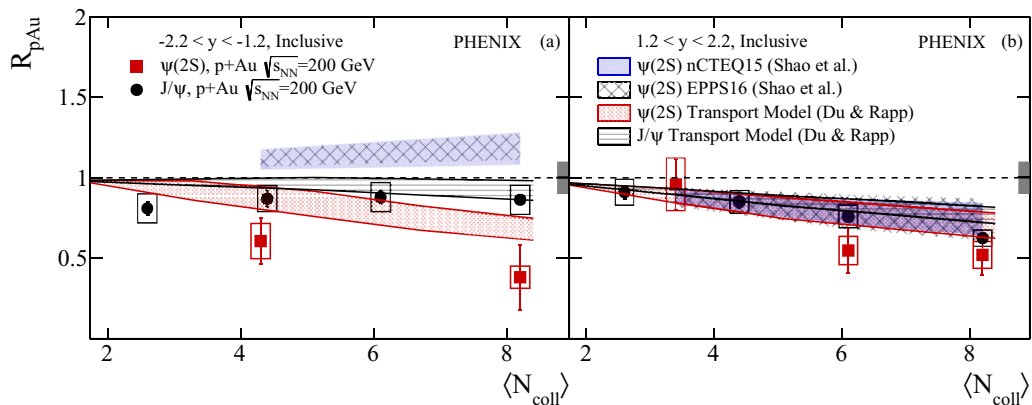

FIG. 6. The $\psi(2S)$ [solid (red) squares] and J/ψ [solid (black) circles] [24] nuclear-modification factors as a function of $\langle N_{coll} \rangle$ in $p + Au$ collisions at (a) backward and (b) forward rapidity are shown with $\psi(2S)$ EPPS16 [13] and nCTEQ15 [14] nPDF predictions. Also shown are the $\psi(2S)$ and J/ψ transport-model predictions [53]. The error boxes (bars) represent point-to-point correlated (uncorrelated) uncertainties for each data point. The Type-C global systematic uncertainty is indicated by the shaded box on the right side of the figure and includes the BBC efficiency and bias-correction uncertainties. See text for descriptions of the model predictions.
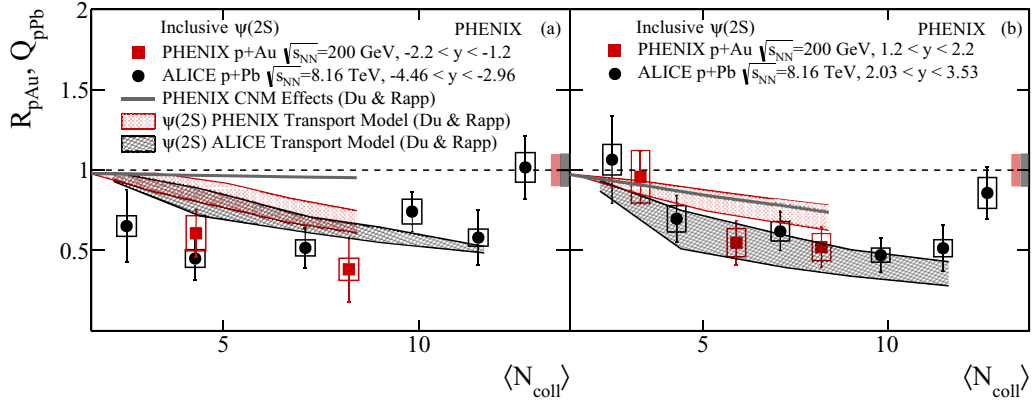
FIG. 7. The PHENIX [solid (red) squares] and ALICE [solid (black) circles] $\psi(2S)$ nuclear-modification factors as a function of $\langle N_{coll} \rangle$ in $p+$ Au collisions at (a) backward and (b) forward rapidity. The error boxes (bars) represent point-to-point correlated (uncorrelated) uncertainties for each data point. The Type-C global systematic uncertainty is indicated by the shaded box on the right side of the figure and includes the BBC efficiency and bias-correction uncertainties. Descriptions of the model predictions are provided in the text.

2.9σ effect. The $\psi(2S)$ antishadowing predictions provided by Shao *et al.* shown in Fig. 6(a) do not predict the suppression. These predictions are purely antishadowing and do not contain any additional CNM effects, such as nuclear absorption. The measured J/ψ nuclear modification is nearly constant as a function of centrality. This behavior may arise as a trade-off between the competing effects of nuclear-thickness-dependent antishadowing enhancement and nuclear-absorption suppression [15,30]. Figure 6(a) also shows a comparison to TM predictions at backward rapidity, and final-state effects and nuclear absorption are expected to be important. In addition to gluon antishadowing predictions, the TM includes a nuclear-absorption estimate for both the $\psi(2S)$ and J/ψ. The TMs underpredict the suppression but describe the relative modification well and indicate that the $\psi(2S)$ suppression in $p+$ Au collisions is consistent with final-state effects. The individual contributions from CNM effects alone can be seen in Fig. 5, which shows that hot-nuclear-matter effects are the predominant

source of the stronger $\psi(2S)$ suppression at backward rapidity.

Figure 7 shows the PHENIX $\psi(2S)$ and the ALICE $\psi(2S)$ nuclear-modification factors [24] as a function of $\langle N_{coll} \rangle$. Please refer to the ALICE publication [24] for more information regarding the notation Q_{pPb} used for the nuclear-modification factor measurements. Due to the higher energy at the LHC, the nucleon-nucleon cross section is larger, which leads to a larger range of $\langle N_{coll} \rangle$ values for the ALICE data. The Bjorken-x values probed in the target at LHC energies are smaller than the values probed at RHIC energies. Additionally, the Q^2 values are higher at LHC energies due to the larger mean p_T values. The Du and Rapp TM predictions [53] are compared with the experimental data. At backward rapidity where hot-nuclear-matter effects are dominant, both TMs predict a similar degree of suppression.

Figure 8 compares the $\psi(2S)$ to J/ψ ratios for PHENIX and ALICE [24] as a function of $\langle N_{coll} \rangle$. The PHENIX $\psi(2S)$ to J/ψ ratio in $p+p$ collisions is shown at $\langle N_{coll} \rangle = 1$. By

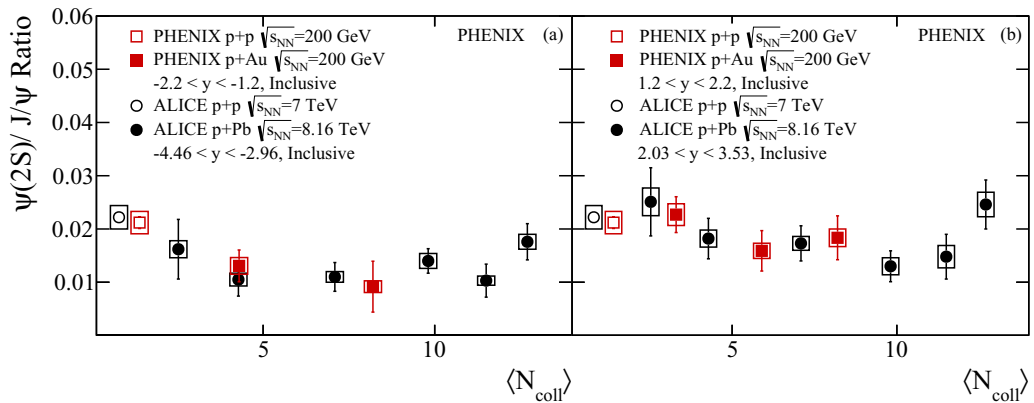FIG. 8. The PHENIX [solid (red) squares] $\psi(2S)$ to J/ψ ratios as a function of $\langle N_{coll} \rangle$ in $p+$ Au collisions at (a) backward and (b) forward rapidity are compared with ALICE [solid (black) circles] ratios in $p+$ Pb collisions [24]. The data points at $\langle N_{coll} \rangle = 1$ are the equivalent PHENIX [open (red) squares] and ALICE [65] [open (black) circles] ratios in $p+p$ collisions. The error boxes (bars) represent point-to-point correlated (uncorrelated) uncertainties for each data point, and includes the BBC efficiency and bias-correction uncertainties.
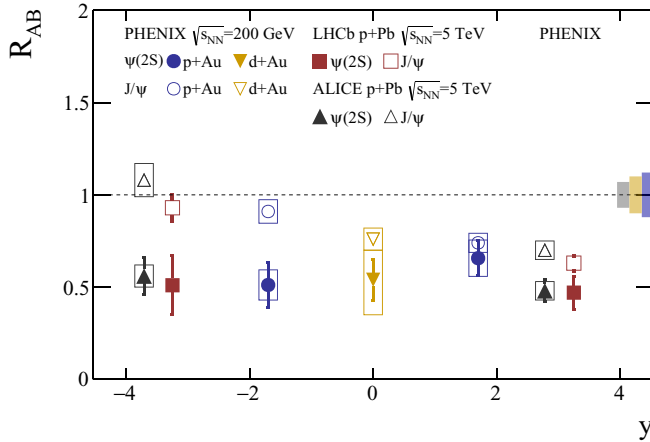
FIG. 9. The centrality- and p_T-integrated J/ψ and $\psi(2S)$ nuclear-modification factors as a function of rapidity are shown for small systems at PHENIX [downward (gold) triangles [8] and (blue) circles], LHCb [(red) squares [10,25]], and ALICE [upward (black) triangles [9,20]]. The error boxes (bars) for the measurements represent point-to-point correlated (uncorrelated) uncertainties for each data point. The Type-C global systematic uncertainty is indicated by the shaded box on the right side of the figure, and includes the BBC efficiency, $\langle N_{\mathrm{coll}} \rangle$, and bias-correction uncertainties.

taking the ratio, any initial-state effects are expected to largely cancel because contributions to the charmonium modification should be similar between the two states. At backward rapidity, a stronger suppression is seen for the $\psi(2S)$ with respect to the J/ψ relative to forward rapidity, which can be observed in comparison with the $p + p$ reference measurement. The observed decrease of the $p + A$ ratio with respect to the ratio in $p + p$ collisions strongly suggests the presence of final-state effects in $p + A$ collisions. Perhaps surprisingly, the comparison of PHENIX and ALICE $\psi(2S)$ to J/ψ ratios indicates that final-state effects at RHIC and LHC energies are similar. This could be due to a combination of hotter temperature and longer lifetime of quark-gluon plasma forming at LHC energies and a shorter exposure to the medium due to higher mean p_T. Note that, in $p + p$ collisions, the $\psi(2S)$ to J/ψ ratio from world data shows no clear energy dependence as a function of center-of-mass energy [32].

Figure 9 presents measurements of the J/ψ and $\psi(2S)$ nuclear-modification factors in small-system collision systems from three different experimental collaborations. The PHENIX measurements are shown for $d + \mathrm{Au}$ collisions [8] and $p + \mathrm{Au}$ collisions. The LHCb [10,25] and AL-ICE [9,20] measurements are shown for $p + \mathrm{Pb}$ collisions. At forward rapidity, the J/ψ and $\psi(2S)$ suppressions are similar, suggesting that initial-state effects dominate charmonium modification. At backward rapidity, the results show a larger differential suppression. The nuclear-modification results from PHENIX, LHCb, and ALICE are consistent with increasing final-state effects in small systems for rapidities in the A-going direction.

V. SUMMARY AND CONCLUSIONS

The results presented in this paper address initial- and final-state effects on charmonium production in $p + p$, $p + \mathrm{Al}$, and $p + \mathrm{Au}$ collisions at $\sqrt{s_{NN}} = 200$ GeV. The J/ψ and $\psi(2S)$ nuclear-modification results and the measured $\psi(2S)$ to J/ψ ratios are shown for $p + \mathrm{Au}$ collisions as a function of $\langle N_{\mathrm{coll}} \rangle$. The p_T- and centrality-integrated J/ψ and $\psi(2S)$ nuclear-modification factors in $p + \mathrm{Au}$ and $p + \mathrm{Al}$ collisions were also presented as a function of rapidity.

At forward rapidity, the reweighted EPPS16 [13] and nCTEQ15 [14] nPDF predictions predictions slightly underestimate the suppression of the $\psi(2S)$ nuclear-modification measurements. Initial-state effects are expected to produce similar modification for the J/ψ and $\psi(2S)$ states. The data show the $\psi(2S)$ suppression is similar to the J/ψ suppression in the most central collisions at forward rapidity, suggesting the dominant contribution to nuclear-modification is gluon shadowing. At backward rapidity, the antishadowing predictions alone cannot reproduce the $\psi(2S)$ nuclear-modification data and suggests that additional effects beyond gluon antishadowing are present.

In a previous PHENIX publication [30], it was shown that the centrality-dependent suppression seen in the J/ψ nuclear modification in $p + \mathrm{Au}$ collisions at backward rapidity was consistent with a trade-off between gluon-antishadowing and nuclear absorption. There will also be a trade-off in the $p + \mathrm{Al}$ system between absorption and antishadowing, although both will be weaker. No suppression was observed at backward rapidity for the J/ψ nuclear modification in $p + \mathrm{Al}$ collisions. The difference in suppression between the J/ψ and $\psi(2S)$ states is suggestive of final-state effects, although a strong statement is not possible due to the large experimental uncertainties.

Comparing the TM predictions with the data, the relative suppression between J/ψ and $\psi(2S)$ is well described, although the overall suppression is underestimated. As seen in Fig. 5(b), the model predicts slightly stronger suppression for the $\psi(2S)$ at forward rapidity due to a small final-state effect. Also seen in Fig. 5(a), at backward rapidity the model predicts significantly more suppression of the $\psi(2S)$ than the J/ψ. This is due to a stronger final-state effect for the $\psi(2S)$ because contributions from CNM effects are the same in both the $\psi(2S)$ and J/ψ TM predictions.

At backward rapidity, the PHENIX and ALICE $\psi(2S)$ nuclear modification results are surprisingly similar. The TM calculations at the two energies reproduce this well. The PHENIX $\psi(2S)$ to J/ψ ratio was compared with the ALICE ratio as a function of $\langle N_{\mathrm{coll}} \rangle$ to cancel most of the modifications due to initial-state effects, which are expected to be different at the two energies. The PHENIX and ALICE $\psi(2S)$ to J/ψ ratio measurements follow the same trend at backward rapidity, indicating that final-state effects on inclusive charmonium states appears to be very similar at RHIC and LHC energies.

In comparing PHENIX J/ψ and $\psi(2S)$ nuclear modification with LHCb and ALICE results, at forward rapidity the $\psi(2S)$ nuclear modification is slightly more suppressed than

the J/ψ nuclear modification at the most forward rapidity, suggesting that initial-state effects are the dominant contribution. At backward rapidity, a clear trend is seen where the $\psi(2S)$ is more suppressed than the J/ψ. This observed behavior reported by three different experiments is consistent with transport models that include hot-nuclear-matter effects in the A-going direction.

[1] J. L. Nagle and W. A. Zajc, Small system collectivity in relativistic hadronic and nuclear collisions, Annu. Rev. Nucl. Part. Sci. **68**, 211 (2018).

[2] V. Khachatryan *et al.* (CMS Collaboration), Observation of long-range near-side angular correlations in proton-proton collisions at the LHC, J. High Energy Phys. 09 (2010) 091.

[3] B. Abelev *et al.* (ALICE Collaboration), Long-range angular correlations on the near and away side in p-Pb collisions at $\sqrt{s_{NN}} = 5.02$ TeV, Phys. Lett. B **719**, 29 (2013).

[4] L. Adamczyk *et al.* (STAR Collaboration), Measurement of elliptic flow of light nuclei at $\sqrt{s_{NN}} = 200$, 62.4, 39, 27, 19.6, 11.5, and 7.7 GeV at the BNL Relativistic Heavy Ion Collider, Phys. Rev. C **94**, 034908 (2016).

[5] M. Aaboud *et al.* (ATLAS Collaboration), Measurement of multi-particle azimuthal correlations in pp, $p+$Pb and low-multiplicity Pb + Pb collisions with the ATLAS detector, Eur. Phys. J. C **77**, 428 (2017).

[6] C. Aidala *et al.* (PHENIX Collaboration), Creation of quark-gluon plasma droplets with three distinct geometries, Nat. Phys. **15**, 214 (2019).

[7] U. A. Acharya *et al.* (PHENIX Collaboration), Kinematic dependence of azimuthal anisotropies in $p + $Au, $d + $Au, ^{3}He $+$Au at $\sqrt{s_{NN}} = 200$ GeV, Phys. Rev. C **105**, 024901 (2022).

[8] A. Adare *et al.* (PHENIX Collaboration), Nuclear Modification of ψ', χ_c, and J/ψ Production in $d +$ Au Collisions at $\sqrt{s_{NN}} = 200$ GeV, Phys. Rev. Lett. **111**, 202301 (2013).

[9] B. B. Abelev *et al.* (ALICE Collaboration), Suppression of $\psi(2S)$ production in p-Pb collisions at $\sqrt{s_{NN}} = 5.02$ TeV, J. High Energy Phys. 12 (2014) 073.

[10] R. Aaij *et al.* (LHCb Collaboration), Study of $\psi(2S)$ production and cold nuclear matter effects in pPb collisions at $\sqrt{s_{NN}} = 5$ TeV, J. High Energy Phys. 03 (2016) 133.

[11] A. Adare *et al.* (PHENIX Collaboration), Transverse-momentum dependence of the J/ψ nuclear modification in $d +$ Au collisions at $\sqrt{s_{NN}} = 200$ GeV, Phys. Rev. C **87**, 034904 (2013).

[12] N. Brambilla *et al.*, Heavy quarkonium: Progress, puzzles, and opportunities, Eur. Phys. J. C **71**, 1534 (2011).

[13] K. J. Eskola, P. Paakkinen, H. Paukkunen, and C. A. Salgado, EPPS16: Nuclear parton distributions with LHC data, Eur. Phys. J. C **77**, 163 (2017).

[14] K. Kovařík, A. Kusina, T. Jezo, D. B. Clark, C. Keppel, F. Lyonnet, J. G. Morfin, F. I. Olness, J. F. Owens, I. Schienbein, and J. Y. Yu, nCTEQ15- Global analysis of nuclear parton distributions with uncertainties in the CTEQ framework, Phys. Rev. D **93**, 085037 (2016).

[15] D. C. McGlinchey, A. D. Frawley, and R. Vogt, Impact parameter dependence of the nuclear modification of J/ψ production in $d +$ Au collisions at $\sqrt{s_{NN}} = 200$ GeV, Phys. Rev. C **87**, 054910 (2013).

[16] F. Arleo, P. B. Gossiaux, T. Gousset, and J. Aichelin, Charmonium suppression in pA collisions, Phys. Rev. C **61**, 054906 (2000).

[17] I. Vitev, Non-Abelian energy loss in cold nuclear matter, Phys. Rev. C **75**, 064906 (2007).

[18] J. W. Cronin, H. J. Frisch, M. J. Shochet, J. P. Boymond, R. Mermod, P. A. Piroue, and R. L. Sumner, Production of hadrons with large transverse momentum at 200, 300, and 400 GeV, Phys. Rev. D: Part. Fields **11**, 3105 (1975).

[19] J. Adam *et al.* (ALICE Collaboration), Centrality dependence of inclusive J_ψ production in p-Pb collisions at $\sqrt{s_{NN}} = 5.02$ TeV, J. High Energy Phys. 11 (2015) 127.

[20] B. B. Abelev *et al.* (ALICE Collaboration), J/ψ production and nuclear effects in p-Pb collisions at $\sqrt{S_{NN}} = 5.02$ TeV, J. High Energy Phys. 02 (2014) 073.

[21] G. Aad *et al.* (ATLAS Collaboration), Measurement of differential J/ψ production cross sections and forward-backward ratios in $p +$ Pb collisions with the ATLAS detector, Phys. Rev. C **92**, 034904 (2015).

[22] M. Aaboud *et al.* (ATLAS Collaboration), Measurement of quarkonium production in proton-lead and proton-proton collisions at 5.02 TeV with the ATLAS detector, Eur. Phys. J. C **78**, 171 (2018).

[23] J. Adam *et al.* (ALICE Collaboration), Centrality dependence of $\psi(2S)$ suppression in *p*-Pb collisions at $\sqrt{s_{NN}} = 5.02$ TeV, J. High Energy Phys. 06 (2016) 050.

[24] S. Acharya *et al.* (ALICE Collaboration), Centrality dependence of J/ψ and $\psi(2S)$ production and nuclear modification in *p*-Pb collisions at $\sqrt{s_{NN}} = 8.16$ TeV, J. High Energy Phys. 02 (2021) 002.

[25] R. Aaij *et al.* (LHCb Collaboration), Study of J/ψ production and cold nuclear matter effects in pPb collisions at $\sqrt{s_{NN}} = 5$ TeV, J. High Energy Phys. 02 072 (2014).

[26] A. M. Sirunyan *et al.* (CMS Collaboration), Measurement of prompt and nonprompt J/ψ production in *pp* and *p*Pb collisions at $\sqrt{s_{NN}} = 5.02$ TeV, Eur. Phys. J. C **77**, 269 (2017).

[27] A. M. Sirunyan *et al.* (CMS Collaboration), Measurement of prompt $\psi(2S)$ production cross sections in proton-lead and proton-proton collisions at $\sqrt{s_{NN}} = 5.02$ TeV, Phys. Lett. B **790**, 509 (2019).

[28] A. Adare *et al.* (PHENIX Collaboration), Ground and excited charmonium state production in $p + p$ collisions at $\sqrt{s} = 200$ GeV, Phys. Rev. D **85**, 092004 (2012).

[29] A. Adare *et al.* (PHENIX Collaboration), Cold Nuclear Matter Effects on J/ψ Yields as a Function of Rapidity and Nuclear Geometry in Deuteron-Gold Collisions at $\sqrt{s_{NN}} = 200$ GeV, Phys. Rev. Lett. **107**, 142301 (2011).

[30] U. Acharya *et al.* (PHENIX Collaboration), Measurement of J/ψ at forward and backward rapidity in $p + p$, $p + $Al, $p + $Au, and ^{3}He $+$Au collisions at $\sqrt{s_{NN}} = 200$ GeV, Phys. Rev. C **102**, 014902 (2020).

[31] L. Adamczyk *et al.* (STAR Collaboration), J/ψ production at low transverse momentum in $p + p$ and $d + $Au collisions at $\sqrt{s_{NN}} = 200$ GeV, Phys. Rev. C **93**, 064904 (2016).

[32] A. Adare *et al.* (PHENIX Collaboration), Measurement of the relative yields of $\psi(2S)$ to $\psi(1S)$ mesons produced at forward and backward rapidity in $p + p$, $p + $Al, $p + $Au, and ^{3}He $+$Au collisions at $\sqrt{s_{NN}} = 200$ GeV, Phys. Rev. C **95**, 034904 (2017).

[33] H. Akikawa Jr. *et al.* (PHENIX Collaboration), PHENIX muon arms, Nucl. Instrum. Methods Phys. Res., Sect. A **499**, 537 (2003).

[34] S. Adachi *et al.*, Trigger electronics upgrade of PHENIX muon tracker, Nucl. Instrum. Methods Phys. Res., Sect. A **703**, 114 (2013).

[35] C. Aidala *et al.*, The PHENIX forward silicon vertex detector, Nucl. Instrum. Methods Phys. Res., Sect. A **755**, 44 (2014).

[36] M. Allen *et al.* (PHENIX Collaboration), PHENIX inner detectors, Nucl. Instrum. Methods Phys. Res., Sect. A **499**, 549 (2003).

[37] A. Adare *et al.* (PHENIX Collaboration), Centrality categorization for $R_{p(d)+A}$ in high-energy collisions, Phys. Rev. C **90**, 034902 (2014).

[38] J. E. Gaiser, Charmonium spectroscopy from radiative decays of the J/ψ and ψ', Ph.D. thesis, SLAC, 1982, https://inspirehep.net/literature/183554.

[39] C. Aidala *et al.* (PHENIX Collaboration), Measurements of $\mu\mu$ pairs from open heavy flavor and Drell-Yan in $p + p$ collisions at $\sqrt{s} = 200$ GeV, Phys. Rev. D **99**, 072003 (2019).

[40] A. Adare *et al.* (PHENIX Collaboration), Heavy quark production in $p + p$ and energy loss and flow of heavy quarks in Au $+$ Au collisions at $\sqrt{s_{NN}} = 200$ GeV, Phys. Rev. C **84**, 044905 (2011).

[41] R. Choudhury *et al.*, Technical design report of the forward silicon vertex tracker (2007), https://www.osti.gov/biblio/912839.

[42] M. Tanabashi *et al.* (Particle Data Group), Review of particle physics, Phys. Rev. D **98**, 030001 (2018).

[43] Y. H. Leung (PHENIX Collaboration), Measurements of charm, bottom, and Drell-Yan via dimuons in $p + p$ and $p + $Au collisions at $\sqrt{s_{NN}} = 200$ GeV with PHENIX at RHIC, Nucl. Phys. A **982**, 695 (2019).

[44] T. Sjöstrand, S. Mrenna, and P. Z. Skands, A brief introduction to PYTHIA8.1, Comput. Phys. Commun. **178**, 852 (2008).

[45] S. Agostinelli *et al.* (GEANT4 Collaboration), GEANT4: A simulation toolkit, Nucl. Instrum. Methods Phys. Res., Sect. A **506**, 250 (2003).

[46] A. Drees, B. Fox, Z. Xu, and H. Huang, Results from Vernier scans at RHIC during the *pp* Run 2001-2002, Conf. Proc. C **030512**, 1688 (2003).

[47] C. Aidala *et al.* (PHENIX Collaboration), *B*-meson production at forward and backward rapidity in $p + p$ and Cu $+$ Au collisions at $\sqrt{s_{NN}} = 200$ GeV, Phys. Rev. C **96**, 064901 (2017).

[48] S. S. Adler *et al.* (PHENIX Collaboration), Mid-Rapidity Neutral Pion Production in Proton Proton Collisions at $\sqrt{s} = 200$ GeV, Phys. Rev. Lett. **91**, 241803 (2003).

[49] U. Acharya *et al.* (PHENIX Collaboration), Polarization and cross section of midrapidity J/ψ production in $p + p$ collisions at $\sqrt{s} = 510$ GeV, Phys. Rev. D **102**, 072008 (2020).

[50] B. Abelev *et al.* (ALICE Collaboration), J/ψ Polarization in *pp* Collisions at $\sqrt{s} = 7$ TeV, Phys. Rev. Lett. **108**, 082001 (2012).

[51] R. Aaij Jr. *et al.* (LHCb Collaboration), Measurement of J/ψ polarization in *pp* collisions at $\sqrt{s} = 7$ TeV, Eur. Phys. J. C **73**, 2631 (2013).

[52] S. Chatrchyan Jr. *et al.* (CMS Collaboration), Measurement of the prompt J/ψ and $\psi(2s)$ polarizations in *pp* collisions at $\sqrt{s} = 7$ TeV, Phys. Lett. B **727**, 381 (2013).

[53] X. Du and R. Rapp, In-medium charmonium production in proton-nucleus collisions, J. High Energy Phys. 03 (2019) 015.

[54] K. J. Eskola, H. Paukkunen, and C. A. Salgado, EPS09: A new generation of NLO and LO nuclear parton distribution functions, J. High Energy Phys. 04 (2009) 065.

[55] R. Vogt, Cold nuclear matter effects on J/ψ and Υ production at the LHC, Phys. Rev. C **81**, 044903 (2010).

[56] A. Adare *et al.* (PHENIX Collaboration), Pseudorapidity Dependence of Particle Production and Elliptic Flow in Asymmetric Nuclear Collisions of $p + $Al, $p + $Au, $d + $Au, and ^{3}He $+$Au at $\sqrt{s_{NN}} = 200$ GeV, Phys. Rev. Lett. **121**, 222301 (2018).

[57] A. Kusina, J.-P. Lansberg, I. Schienbein, and H.-S. Shao, Gluon Shadowing in Heavy-Flavor Production at the LHC, Phys. Rev. Lett. **121**, 052004 (2018).

[58] H.-S. Shao, HELAC-Onia: An automatic matrix element generator for heavy quarkonium physics, Comput. Phys. Commun. **184**, 2562 (2013).

[59] H.-S. Shao, HELAC-Onia 2.0: An upgraded matrix-element and event generator for heavy quarkonium physics, Comput. Phys. Commun. **198**, 238 (2016).

[60] J.-P. Lansberg and H.-S. Shao, Towards an automated tool to evaluate the impact of the nuclear modification of the gluon

density on quarkonium, D and B meson production in proton-nucleus collisions, Eur. Phys. J. C **77**, 1 (2017).

[61] A. Kusina, J.-P. Lansberg, I. Schienbein, and H.-S. Shao, Reweighted nuclear PDFs using heavy-flavor production data at the LHC, Phys. Rev. D **104**, 014010 (2021).

[62] C. Loizides, J. Kamin, and D. d'Enterria, Improved Monte Carlo Glauber predictions at present and future nuclear colliders, Phys. Rev. C **97**, 054910 (2018); **99**, 019901(E) (2019).

[63] H.-S. Shao, Probing impact-parameter dependent nuclear parton densities from double parton scatterings in heavy-ion collisions, Phys. Rev. D **101**, 054036 (2020).

[64] X. Zhao and R. Rapp, Charmonium in medium: From correlators to experiment, Phys. Rev. C **82**, 064905 (2010).

[65] B. B. Abelev *et al.* (ALICE Collaboration), Measurement of quarkonium production at forward rapidity in pp collisions at $\sqrt{s} = 7$ TeV, Eur. Phys. J. C **74**, 2974 (2014).